PAPER

Check for updates

Moisture-driven electric power generation using graphene-based hydrogels for sustained power output and self-powered sensing

Nishadi M. Bandara, [ID] [a] Jinzhou Liu,[b] Brenden Ferland, [ID] [b] Mahdad Mahmoudi[a] and Douglas H. Adamson [ID] *[ab]

Moist electric generators (MEGs) produce electric power from hydration gradients and have been identified as a promising sustainable technology for advanced energy systems. This article reports the fabrication of a graphene-templated poly(acrylic acid) (PAA) hydrogel MEG with a gradient distribution of PAA swelling resulting from variations in polymer confinement. The MEG delivers an open-circuit voltage of 0.78 V for over 120 hours under ambient environmental conditions with a power density of 62 mW m^{-2}. The MEG effectively operates at temperatures as low as -25 °C. A current output of 780 μA has been achieved through a parallel configuration of MEG elements, and an output of 18 V has been achieved using a series configuration. The electric output of the MEGs can be scaled and is shown to power various commercial electronics, including LEDs, an 8-digit calculator, and a humidity sensor with an LCD screen. Additionally, the MEG is shown to perform as a self-powered tactile sensor.

1. Introduction

Green energy-harvesting technologies have attracted significant attention as viable approaches to reduce our reliance on fossil-fuel-based energy systems.[1,2] Numerous technologies utilizing triboelectricity,[3] piezoelectricity,[4] thermoelectricity,[5] and moist electric generation[6] have been proposed to convert various forms of energy into electrical power. Among these various energy harvesting techniques, moist electric generation (MEG) has emerged as a promising approach for electric power generation.[7] In this article, we introduce and demonstrate a MEG device templated by a spontaneously formed graphene-stabilized emulsion with an inherent polymer swelling gradient arising from a gradient of emulsion droplet sizes.

Moisture-enabled electricity generation involves converting chemical energy into electrical energy.[8] This process is facilitated by mechanisms such as ion drift[8,9] induced by concentration gradients, streaming potential,[10,11] or surface charge potential,[12,13] which arise from the interaction between moisture and hygroscopic materials within moist electric generating devices. At the heart of these materials is an ion gradient that requires careful synthesis or processing to establish. A typical MEG comprises a hygroscopic material containing functional groups capable of ionizing upon exposure to moisture, coupled with a pair of inert electrodes to facilitate electron transmission in external circuits.[14] When the MEG is subjected to moisture, the

hygroscopic materials absorb water, ionizing the hydrophilic functional groups, leading to a gradient of positive ions (H$^+$). These ions diffuse in response to a concentration gradient, generating an electric potential between the two electrodes. The power output of MEGs that rely on ion diffusion is predominantly determined by their water-capturing capacity and the constructed gradient. Enhancing water absorption capacity enables MEGs to harness additional chemical energy, which ultimately results in an elevated power output.[15] However, excessive water uptake can induce rapid equilibrium, resulting in diminished electrical output. The challenge is to simultaneously achieve efficient water capture and maintain a stable water gradient over the long term.

Various strategies have been employed to enhance moisture absorption while maintaining a sustained moisture gradient. For example, composites with a gradient distribution of hydrophilic functional groups have been engineered to facilitate self-sustained electric generation through gradient-driven water adsorption, subsequent ionization of the functional groups, and directional ion diffusion. Qu *et al.* developed a strategy termed "moisture–electric annealing" to induce a gradient distribution of oxygen-containing functional groups within oxidized graphene.[16] The resulting gradient graphene oxide film demonstrated a voltage output of 35 mV, which stimulated considerable research interest and accelerated advancements in this area. Later, a gradient 3D polypyrrole (g-3D-PPy) framework was developed to convert the chemical potential energy into electric power, generating a voltage of 60 mV and a power density of approximately 6.9 mW m^{-2} through an electrolyte-electric annealing (EeA) process.[17] Subsequently, a graphene oxide/sodium polyacrylate (GO/PAAS) composite with a gradient

[a]Department of Chemistry, University of Connecticut, Storrs, Connecticut, USA
[b]Polymer Program, Institute of Materials Science, University of Connecticut, Storrs, Connecticut, USA. E-mail: douglas.adamson@uconn.edu

distribution of functional groups was engineered through directionally controlled laser irradiation, generating a voltage of 0.6 V upon exposure to moisture.[14] In other work, a hygroscopic layer was developed *via* LiCl impregnation into cellulose paper, followed by oxygen plasma treatment, and coupling this layer with a carbon black-loaded cellulon layer to establish a water content gradient yielded an open-circuit voltage of 0.78 V and a stable current of 7.5 μA.[18] However, all the above methods of building functional group gradients involve complex, power-consuming, or difficult-to-scale fabrication processes, hindering their widespread application.[19]

Various strategies, in addition to structural chemical gradients, have been reported to facilitate the migration and transport of mobile ions. One such strategy is to construct moisture gradients, which predominantly involve a semi-open device design, in which one section is sealed to ensure moisture resistance, while the opposing section is highly permeable to facilitate moisture adsorption. This is accomplished by using an electrode that incorporates perforations covering the top surface of a hydrophilic material with a homogeneous chemical composition, while the other electrode fully covers the lower surface.[20–22] Another strategy involves the integration of a bilayer structure utilizing polyanion and polycation films, which generate hydrogen ions (H^+) and chloride ions (Cl^-) upon exposure to moisture. Here, the difference in ion concentration between the two layers establishes the ion concentration gradient that facilitates the diffusion of ions across the bilayer, generating a voltage output.[23,24] However, these methodologies have limitations, including challenges associated with precise synthesis and fabrication processes, device integration complexities, and power matching issues.[25] These drawbacks can hinder the overall efficiency and practicality of the resulting MEGs.

To address these challenges, we have developed a MEG composed of a polyacrylic acid hydrogel templated by a graphene-stabilized oil-in-water emulsion that incorporates a gradient of emulsion droplet sizes. The emulsions are created using a solvent interfacial trapping method (SITM) to exfoliate graphite at oil/water interfaces, where the graphene acts as a 2D surfactant, stabilizing the emulsion.[26–29] SITM is a cost-effective and straightforward method that forms a continuous gradient of droplet sizes due to differences in the ascending velocities of variously sized droplets. The size of the droplet is proportional to its stiffness; varying the sizes of the droplets in contact with the interstitial polymer, after polymerization, controls the degree to which the polymer can swell. We thus create a polymer concentration gradient within the MEG. This structure sustains an ion concentration gradient through asymmetric swelling, maintaining a consistent electric output. Despite its low cost and ease of synthesis, this MEG has electrical properties that are competitive with, or superior to, previously reported MEG materials with far more complicated and costly fabrication techniques.

2. Results and discussion

2.1 Synthesis and fabrication of MEG

The MEG material is a polymerized high internal phase emulsion (poly(HIPE)) with graphene as the surfactant rather than the more common small-molecule surfactants.[26,30] The graphene is produced by the *in situ* exfoliation of natural flake graphite as reported previously.[31] In the system reported here, we have added tannic acid to the aqueous phase to invert the emulsion from a water-in-oil system (without tannic acid) to an oil-in-water emulsion.[32] After forming the emulsion by shaking the solution of heptane and graphite with an aqueous solution including acrylic acid monomer, crosslinker, initiator, tannic acid, and lithium chloride, we polymerized the aqueous continuous phase to form the MEG material.

The MEG material was then sandwiched between a pair of inert electrodes: a silver electrode at the bottom and a platinum electrode at the top, to form the MEG device. The asymmetrical metal electrodes (platinum and silver), commonly used in MEG studies, formed a Schottky contact, promoting unidirectional ion transport and significantly improving the device's performance.[14,33] A schematic is shown in Fig. 1a. A schematic of the synthesis approach is shown in Fig. 1b. Lithium chloride was initially incorporated into the hydrogel as a moisture-trapping and anti-freeze agent based on literature reports.[34] Acrylic acid (AA) was selected as the preferred monomer because poly(acrylic acid) (PAA) has abundant carboxyl groups that can release protons under humid conditions.[35]

2.2 Sphere size gradient

Before the polymerization of the aqueous phase in the oil-in-water emulsion, the graphene-coated oil droplets ascend since the heptane filling them is less dense than the surrounding water. The emulsion's sphere size gradient was established by the larger heptane-filled droplets rising more rapidly than the smaller spheres before the polymerization of the continuous phase, which arrests the ascending movement. This process establishes a cell-size gradient within the material after polymerization, as shown optically in Fig. 2a. Further proof of a sphere size gradient came from thermal gravimetric analysis (TGA) analysis of the MEG, shown in Fig. 2b, where slices of the MEG were analyzed from top to bottom. We hypothesized that in regions with larger spheres, the total interfacial area was less, and so the amount of polymer would be less. In each slice, thermal degradation peaks occurred at 150–275 °C, 325 °C, and 412 °C, corresponding to the decarboxylation, polymer chain degradation, and decomposition of carbonaceous residues, respectively (Fig. S1).[34,35] The amount of polymer increased from layer 1 to 4 as hypothesized.[36] The percent residue that remained after heating to 800 °C, which corresponded to the weight of graphene,[37,38] exhibited the decline from layer 1 to layer 4 (top to bottom). Additionally, Fig. S2 presents the XRD pattern of the hydrogel, confirming its graphitic composition.[22,39]

To further test our hypothesis of the sphere size gradient, we cut a MEG into top and bottom sections and monitored its mass loss over time. The larger pores created by the larger spheres would be expected to show a greater rate of evaporation. Using the following equation, where m_t and m_{dry} are the wet mass of the sample at time t and dry mass, respectively, we plotted % water content *versus* time, as shown in Fig. 2c.

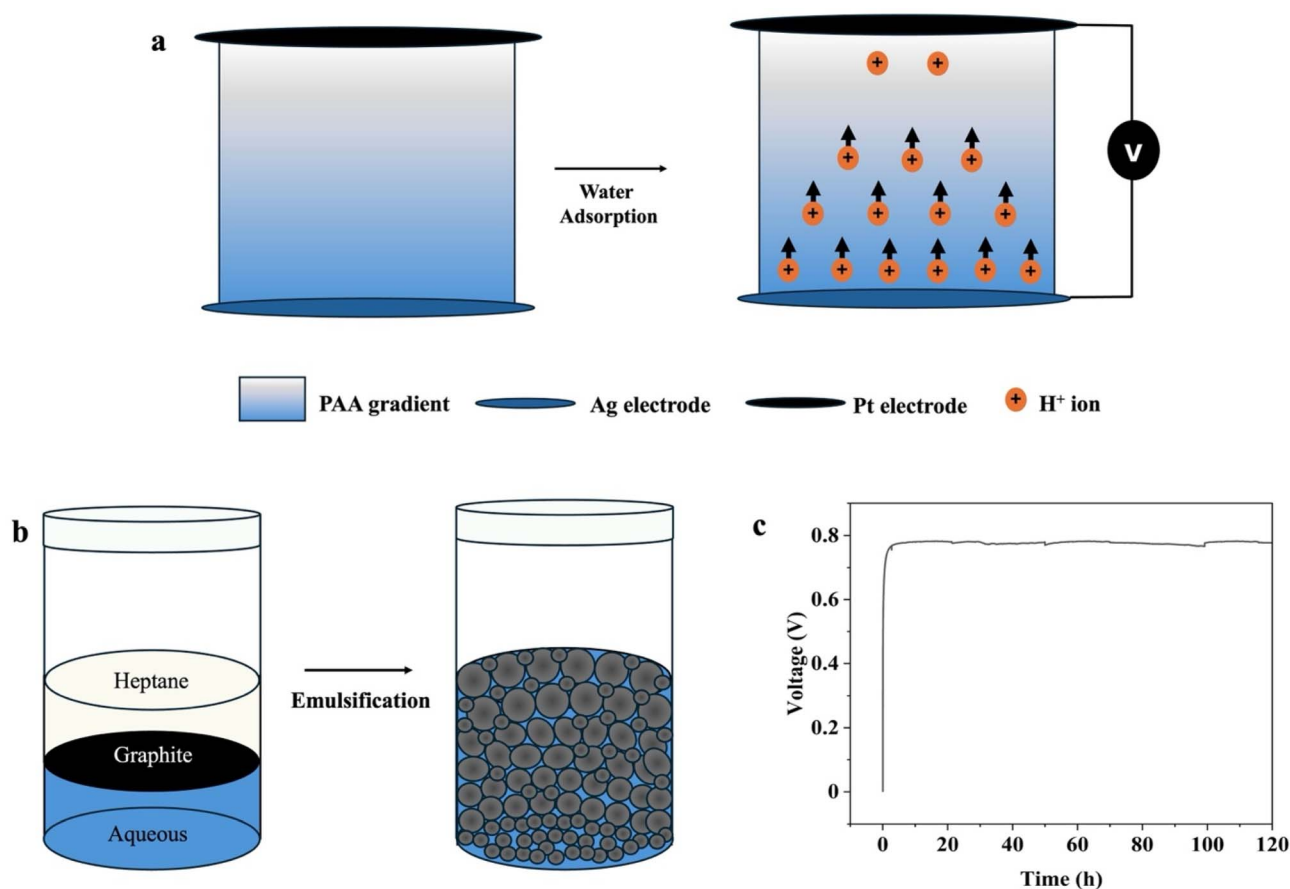$$\text{Water content}(\%) = \frac{(m_t - m_{dry})}{m_t} \times 100 \tag{1}$$

Fig. 1 (a) Schematic illustration of moisture induced electricity generation in the MEG. The hydrogel undergoes asymmetric moisture adsorption; after interacting with moisture, the carboxyl functional groups in PAA are ionized and release mobile protons, generating an electric potential. (b) Schematic showing the hydrogel preparation *via* SITM. (c) The output performance of the MEG under ambient environment of 21 ± 2 °C and $75 \pm 5\%$ RH.
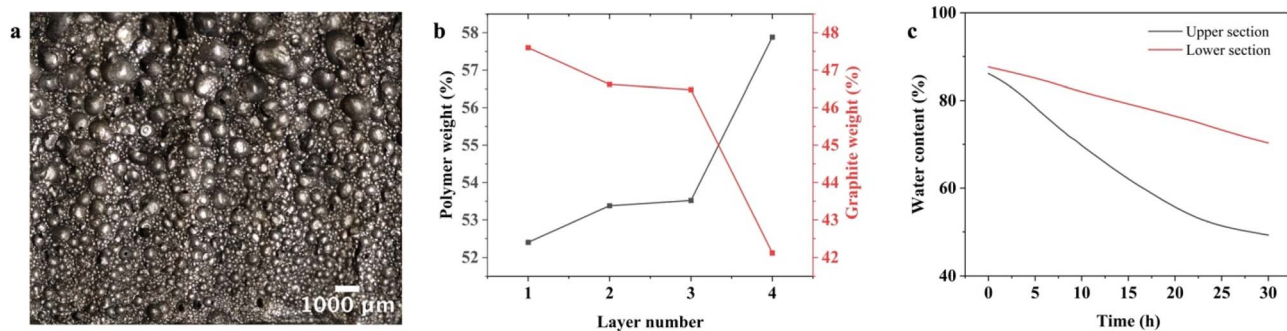

Fig. 2 (a) Digital microscopic image of a vertical cross section of the hydrogel. (b) Variation of graphene weight percentage and polymer weight percentage from layer 1–4 from top to bottom of the hydrogel. (c) Variation in water content percentage over time for a hydrogel sample cut into two halves (top and bottom) at 21 ± 2 °C and $22 \pm 5\%$ RH.

Both halves started with similar water contents ($\sim$85–88%). The upper curve exhibited a steeper decline, indicating faster water loss over time due to the larger pores. The lower curve decreased more gradually, suggesting slower evaporation and better water retention. Our initial hypothesis was that this difference in evaporation rate created the required gradient density in our MEG device. However, as shown in the following section, changes in the relative humidity of the MEG device's environment did not result in the expected changes in electrical properties.

2.3 Electronic properties

Fig. 3a illustrates that the MEG device exhibited a higher voltage output with added LiCl. The hygroscopic salt lithium chloride
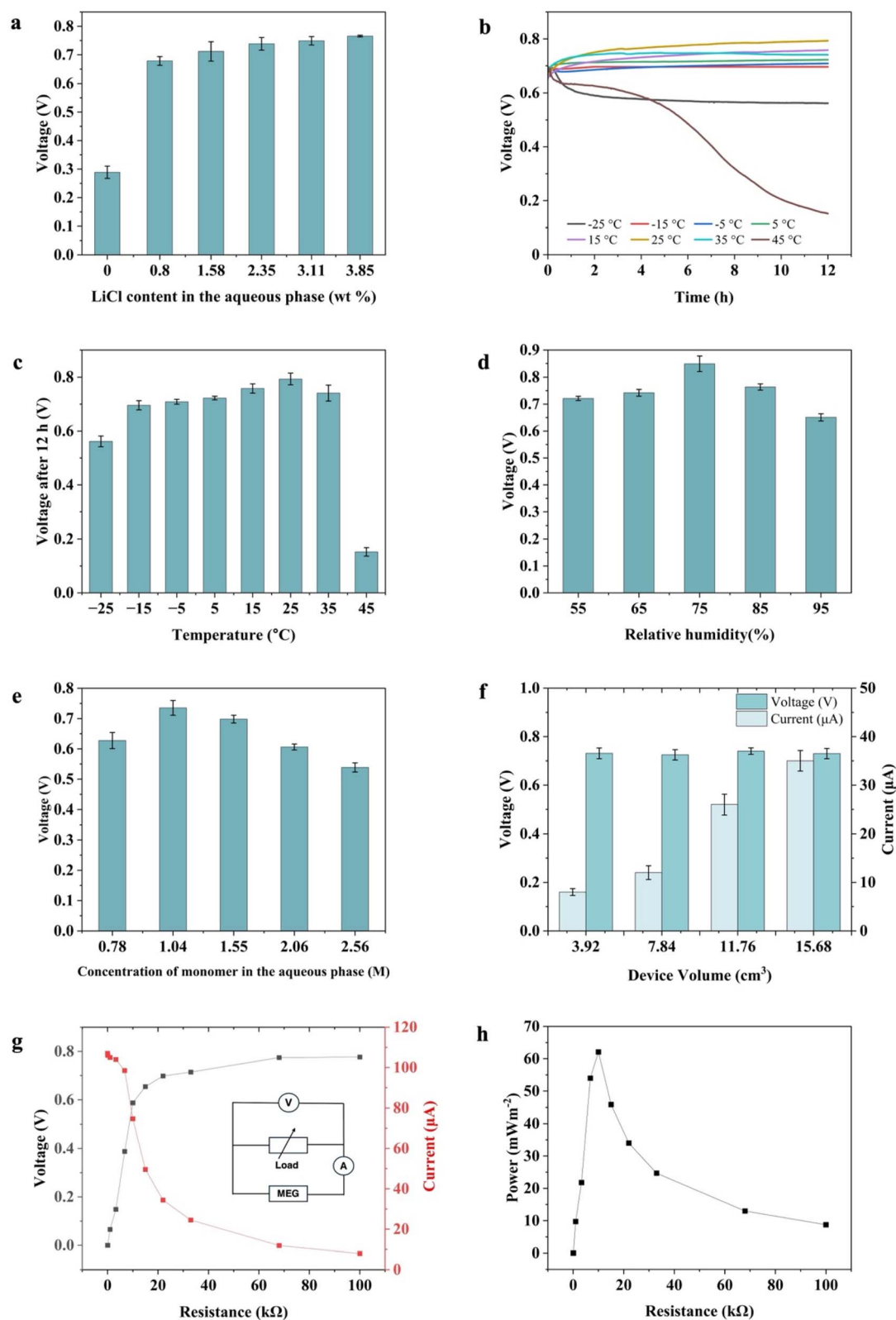
Fig. 3 Potential generated by the MEG device as a function of (a) LiCl content, (b) and (c) temperature, (d) relative humidity, and (e) concentration of monomer in the aqueous phase. (f) The effect of increasing device volume on the potential and current generated by the MEG. (g) voltage output (black), current output (red) as functions of the resistance in a closed circuit. (h) Power generated as a function of an increasing external load.

(LiCl) was added to enhance the hydrogel's moisture adsorption capacity and to provide sufficient mobile ions. In addition, LiCl has been shown to disrupt the hydrogen bonding interactions among the polymer chains due to the Hofmeister effect.[39,40] This disruption has been hypothesized to expand the ion transport channels between the polymer chains, promoting ionic conductivity.[34] We observed that the device's open-circuit voltage remained unchanged with increased LiCl concentration, suggesting that the ionic dynamics may reach a saturation point, beyond which additional LiCl does not substantially affect the overall ionic performance of the device.

Fig. 3b and c illustrate the impact of temperature on the MEG's electrical output. For these studies, hydrogels with identical compositions were allowed to equilibrate until they attained comparable voltage outputs. Their electrical behavior was then monitored over 12 hours at different temperatures. The MEGs were found to generate a significant voltage output over a wide temperature range. The MEG reached its maximum output at a moderate temperature of 25 °C. The loss of potential at high temperature would be expected as the MEG dries out. The performance at low temperature was more surprising. At −25 °C, the moisture in the MEG is frozen, yet it appears that the charge separation remains intact, resulting in a diminished, but still present, electrical potential.

Notably, the device exhibited a stable voltage output of approximately 0.71 V even at −15 °C for 12 hours, probably due to LiCl within the hydrogel composite reducing the freezing point[8,41] of the water within the gel, as illustrated in the thermograms presented in Fig. S3a. Further evidence is provided in Fig. S3b, where the control sample without LiCl showed a sharp decline in voltage output within 2 hours at −5 °C. This discrepancy is attributed to the icing phenomenon that occurs in the absence of LiCl. This frost-resistant property of the hydrogel facilitates effective ion dissociation and transport across the composite at reduced temperatures, expanding its operational range.

Since many MEG devices rely on a humidity gradient, we investigated the humidity-dependent characteristics of our MEGs by exposing the device to varying relative humidity (RH) levels, ranging from 55% to 95% RH. Our results indicated an increase in voltage output as the relative humidity increased from 55% to 75%, as shown in Fig. 3d. However, a decrease in voltage output was observed when the relative humidity exceeded 75%. This result was in contrast to other MEGs that exhibit a marked increase in voltage output with rising humidity levels.[17,40,42] It was also in contrast to our initial hypothesis that our ion gradient was driven by differences in moisture evaporation and absorption rates in our MEG material, as suggested by the results shown in Fig. 2C. Unlike MEGs that operate based on a humidity difference, our measured potential remained steady once equilibrium was reached, suggesting a different mechanism was responsible for the electrical properties observed.

2.4 Mechanism of moist electric generation

We hypothesize that the gradient of sphere diameter in the hydrogel leads to a gradient in the degree of swelling of the interstitial PAA. As the PAA polymer swells, the neighboring spheres are compressed. To test this hypothesis, we estimated the swelling pressure of the polymer and the expected stiffness of the graphene spheres. For our hypothesis to be valid, these values must be in a similar range.

The swelling pressure of the PAA gel is determined by the balance between the elastic energy of the crosslinked polymer and the osmotic pressure of the charged functional groups and counter ions, as described in eqn (2).

$$\Pi_{tot} = \Pi_{mix} + \Pi_{elast} + \Pi_{ion} \tag{2}$$

The last term of the equation, the Donnan term, has been shown to be small when a monovalent salt is added, and so was not considered in our swelling pressure estimate.[43] In our gel, we did not neutralize the carboxylic acid functional groups, and with the added salt, our system was closer to a neutral gel than a typical PAA gel. Based on data from Horkay[43] and using a polymer volume fraction of 0.04 to 0.05, we estimated the swelling pressure to be 7 kPa to 12 kPa.

To show that the estimated swelling pressure of the hydrogel was large enough to distort the graphene-lined spheres but not so large as to collapse them indiscriminately, we next estimated the stiffness of the spheres by estimating the force required to buckle the spheres. As the MEG has an open-cell-foam morphology, the compression of the gas within the spheres was neglected. The classic equation for the buckling of a spherical shell is:

$$p_c = \frac{2E}{\sqrt{3}(1-v^2)}\left(\frac{t}{R}\right)^2 \tag{3}$$

where p_c is the critical buckling pressure, E is the Young's modulus of the shell material, v is Poisson's ratio of the shell material, t is the shell thickness, and R is the radius of the spherical shell. To illustrate the difference between different sized spheres in terms of their resistance to deformation, we calculated the p_c values for spheres of radius 50 μm (100 μm in diameter) and 175 μm (350 μm in diameter) using estimated values of Young's modulus, Poisson's ratio, and shell thickness.

For overlapping graphene sheets, the in-plane stiffness depends on microstructure but is generally reduced from that of defect-free monolayer graphene ($E \approx 1$ TPa). Literature values for graphene paper or multilayer films are typically in the range of 0.8 to 24 GPa, with values as high as 32 GPa reported, depending on alignment and porosity.[44] Here, we used a conservative value of $E = 10$ GPa to reflect a shell made of overlapping nanosheets with moderate order. The Poisson ratio of graphitic carbons is often reported to be between 0.16 and 0.30;[45,46] we used $v = 0.30$. Reports of shell thickness in the literature are largely of graphene oxide systems and range from 200 μm to 350 μm.[47] We set our thickness at 200 nm in the first instance, then repeated the calculation with a value of 20 nm, a lower boundary of what we might expect in our system.

Substituting those values into the equation for p_c, spheres of 50 μm radius gave a p_c value of ∼95 kPa, while 175 μm radius spheres gave a p_c value of ∼7.8 kPa. This suggests the smaller

spheres are roughly 12 times stiffer than the larger ones. Repeating the calculation with an estimated shell thickness of 20 nm gave a p_c value of ~0.95 kPa for the 50 μm radius spheres and p_c = ~0.078 kPa for the larger spheres. Again, there is a factor of 12 between the two values.

Thus, the smaller spheres are predicted to buckle at a pressure ~12 times higher than the larger spheres. This means that, under a given swelling pressure exerted by the PAA hydrogel, 100 μm diameter graphene shells would resist deformation much more strongly than 350 μm diameter shells. The choice of values for both estimates is illustrative rather than absolute. However, the ratio of critical pressures was insensitive to the exact values of E, t, or ν if the same shell material is assumed for both sizes. The calculated factor of 12 difference arises purely from geometric scaling.

The resulting swelling gradient, where the PAA near the larger spheres would be less restrained and thus more swollen than the PAA near the smaller spheres, means the PAA is more dilute near the top of the MEG and more concentrated near the bottom. This polymer concentration gradient in turn leads to an ion concentration gradient, with the more dilute carboxylic groups having a greater degree of ionization in the more swollen PAA. This ion concentration gradient leads to an osmotic pressure gradient that drives the flow of ions from high to low concentration.

Additionally, the TGA data presented in Fig. 2b provide spatially resolved measurements of polymer mass fraction across four sequential layers of the MEG, from the top layer to the bottom layer. Since the swelling pressure in PAA hydrogels scales strongly with polymer volume fraction, this spatial gradient in the polymer content directly implies a corresponding gradient in swelling state throughout the device thickness. Taken together with the optical confirmation of sphere size gradient (Fig. 2a), the differential water evaporation data (Fig. 2c), the mechanically grounded buckling pressure estimates, and the non-monotonic voltage response to PAA concentration (Fig. 3e), provides compelling evidence for the proposed sphere-size-induced swelling gradient mechanism.

As shown in our swelling pressure calculations, the polymer fraction of the hydrogel is a critical parameter of the ultimate swelling pressure. If our proposed mechanism is correct, changing the polymer fraction would significantly affect the measured electrical potential. Fig. 3e confirms this to be the case. There is a marked increase in output voltage from 0.63 V to 0.74 V when the concentration of polyacrylic acid (PAA) is raised to 1.04 M. However, this increase in voltage might also be linked to the enhanced hydration properties of the hydrophilic PAA[48,49] and the increased availability of dissociable protons within the hydrogel matrix rather than being a function of the swelling pressure. However, further increases in PAA concentration led to a reduction in output voltage, despite the rise in available dissociable ions. This result fits with our proposed mechanism, where ideally the swelling pressure is great enough to collapse only the largest spheres. If the swelling pressure is greater than that, a larger fraction of the spheres buckle, decreasing the concentration range of the gradient.

The central role played by the swelling gradient is also supported by the results shown in Fig. 3a. In systems where voltage arises primarily from a hygroscopic gradient driven by salt concentration, one would expect the voltage to continue increasing with increasing LiCl content. The plateau observed here is instead consistent with a mechanism governed primarily by the structural polymer swelling gradient templated by the sphere size distribution. Once sufficient LiCl is incorporated to ensure adequate hydration and bulk ionic mobility throughout the hydrogel, additional LiCl does not alter the underlying swelling-induced polymer concentration gradient, and the voltage correspondingly saturates. LiCl thus plays a permissive rather than a primary role in voltage generation, ensuring the hydrogel remains sufficiently hydrated and ionically conductive to sustain the gradient-driven diffusion potential, but the magnitude of that potential is set by the structural features of the MEG.

The magnitude of the potential and the current as a function of the MEG volume also provided insight into the mechanism behind the electrical properties. As illustrated in Fig. 3f, the open-circuit voltage remained relatively constant regardless of variations in device volume. The MEG's current output, however, increased significantly with increased volume, as the device's volume determined the total number of ions. For this study, the volume of the MEG materials was decreased by cutting standard MEGs into pieces. We found that the potential was not affected by cutting the material longitudinally, suggesting that the separation of charge was relatively uniform throughout the MEG and did not depend on moisture loss or gain rate.

We then measured the voltage and current relative to varying external load resistances, as shown in Fig. 3g. When increasing the external load resistance from 10 Ω to 100 kΩ, the V_{out} initially increased sharply before reaching a plateau, while I_{out} decreased sharply and then approached a constant value. For our standard 15 mL hydrogel MEG, the maximum power density reached 62 mW m^{-2} with a load resistance of 10 kΩ (Fig. 3h). However, as demonstrated in the following investigations, both the potential and current results could be increased considerably.

2.5 Scaling up the electrical performance of the MEG

Our MEGs can be effectively arranged in series or parallel configurations to increase their energy output for various applications. Although a single standard volume MEG generates an output current of 35 μA and an open-circuit voltage of 0.78 V, the voltage was increased through series connections to ~18 V, with 25 series-connected MEGs, with the results shown in Fig. 4a and b. The current could be increased using a parallel arrangement. Fig. 4c shows that 25 MEGs wired in parallel produced an output current of nearly 800 μA. Six devices, arranged in series and parallel connections, produced a continuous electric output of 2.24 V, as shown in Fig. 4d. This demonstrates that the results reported in Fig. 3 are not the maximum values obtainable. This is further demonstrated in
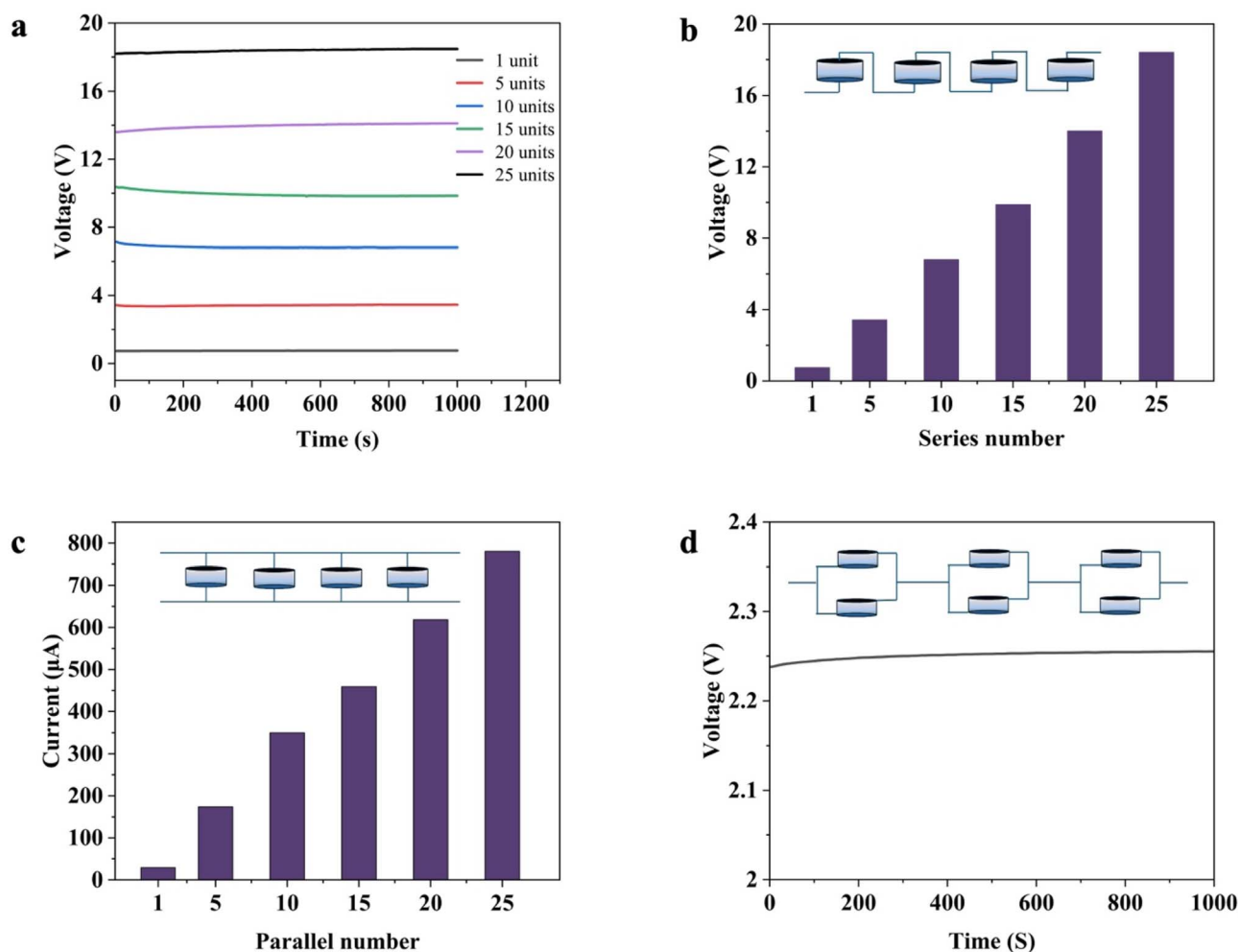
Fig. 4 (a) Electric performance of MEG units with increasing numbers of units wired in series over time. (b) Relationship between output voltage and number of units in series. (c) Relationship between short circuit current and the number of units wired in parallel. (d) Electric performance of a 3 × 2 series and parallel connected MEG bank in an environment at 21 ± 2 °C and 22 ± 5% RH.

the next section, where our MEGs were shown to provide the necessary current and potential for real-world applications.

3. Applications of swelling gradient MEGs

To assess the feasibility of MEGs in real-world applications, we designed and experimentally evaluated their capability to power commercial electronic devices. The approach employed an array of small MEG devices to directly power various electronic devices, thereby demonstrating their utility without the common requirement for supplementary energy storage systems and rectification circuits often needed for energy-harvesting devices such as solar cells, triboelectric nanogenerators, or piezoelectric harvesters.

To create a power source, four MEG units were connected in series. This modest number generated sufficient electric energy to power an 8-digit calculator (1.5 V), enabling it to perform arithmetic operations and display the results on its LCD screen, as shown in Fig. 5a and Video S1. A series connection of four

MEGs could also successfully power a temperature and humidity sensor with an LCD screen (Fig. 5b and Video S2). Electronic devices utilizing MEGs can function over extended periods rather than merely in brief intervals. Moreover, when six MEGs were connected in series, they could illuminate up to eight red light-emitting diodes arranged in parallel (Fig. 5c). This is in contrast to previously reported generators that require additional capacitors and rectifiers to briefly light a single LED.[50]

Moreover, our MEGs could also charge commercial energy storage devices without the need for additional rectifiers and power management circuits. As shown in Fig. 5d, three MEG devices in series charged 10 μF, 100 μF, 470 μF, 1000 μF, and 2200 μF capacitors to 2.4 V in 8 s, 32 s, 99 s, 203 s, and 433 s, respectively. These results illustrate that as capacitor capacitance increases, the time required to charge to a given voltage using MEGs increased, consistent with theoretical charging dynamics. As illustrated in Fig. 5e, capacitors of 10 μF and 100 μF were quickly charged to 0.83 V, 1.64 V, 2.47 V, 2.98 V, and 3.47 V using serially connected MEG banks comprised of 1 to 5
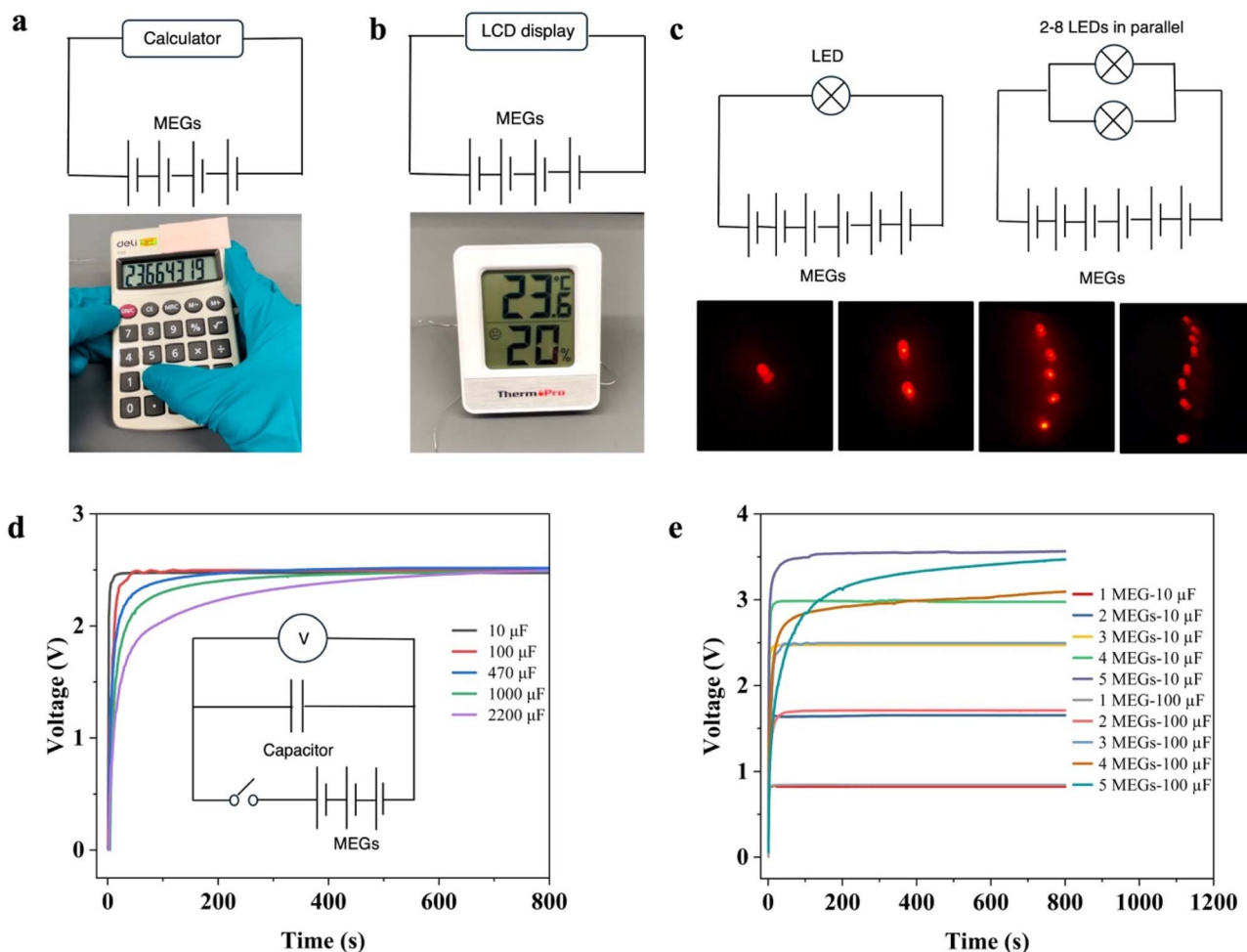
Fig. 5 Demonstration of our MEG devices as power sources for directly powering (a) commercial eight- digit calculator (b) temperature and humidity sensor with an LCD screen and (c) LEDs. (d) voltage–time curves with commercial capacitors of varying capacitance e. voltage–time curves of 10 μF and 100 μF.

units, respectively. As the load voltage (number of MEG devices) increased, it became evident that the time required to charge the 100 μF capacitor was longer than that for the 10 μF capacitor. Hence, our MEG devices offer a sustainable energy solution for small electronic devices.

Finally, applying pressure to the MEG device caused the device to compress and decrease in thickness, elevating the ionic concentration within the hydrogel and reducing the diffusion distance of ions. This interplay resulted in an enhancement of the current output.[51,52] A self-powered sensor was developed based on these characteristics, as illustrated in Fig. 6a. The current output of the MEG varied with the contact pressure of human fingers. Similarly, the hydrogel exhibited varied current output responses when subjected to different compression percentages, as illustrated in Fig. 6b. An increase in compression from 20% to 60% corresponded with a six times enhancement in current from the MEG, demonstrating its suitability for stress-sensing applications. Moreover, Fig. S4 demonstrated that the MEG retained its stable performance even after 400 cycles. A diverse array of sensors exists for

monitoring various stimuli; however, most depend on external power sources. Our MEG shows significant promise as a self-powered tactile sensor with its consistent compressive sensitivity and stable performance under repeated operation.

The self-powered tactile sensor employed the MEG hydrogel element in its as-fabricated form, with no additional materials, layers, or fabrication steps required beyond those described in the Experimental section. The device architecture was identical to that used for energy generation. The PAA/graphene hydrogel was sandwiched between a bottom silver electrode and a top platinum electrode, and a compressive force was applied directly to the exposed top platinum electrode face. The sensing mechanism is iontronic, with an applied pressure compressing the hydrogel, increasing the concentration of ionized carboxylate groups and mobile ions (Li^+, H^+, Cl^-) and reducing the effective ion diffusion distance between the electrodes.[51,52] Both effects increase the ionic current. The response is fully reversible upon pressure release, as the crosslinked PAA hydrogel elastically recovers its original geometry. This mechanism is distinct from piezoelectric sensing (which requires a non-
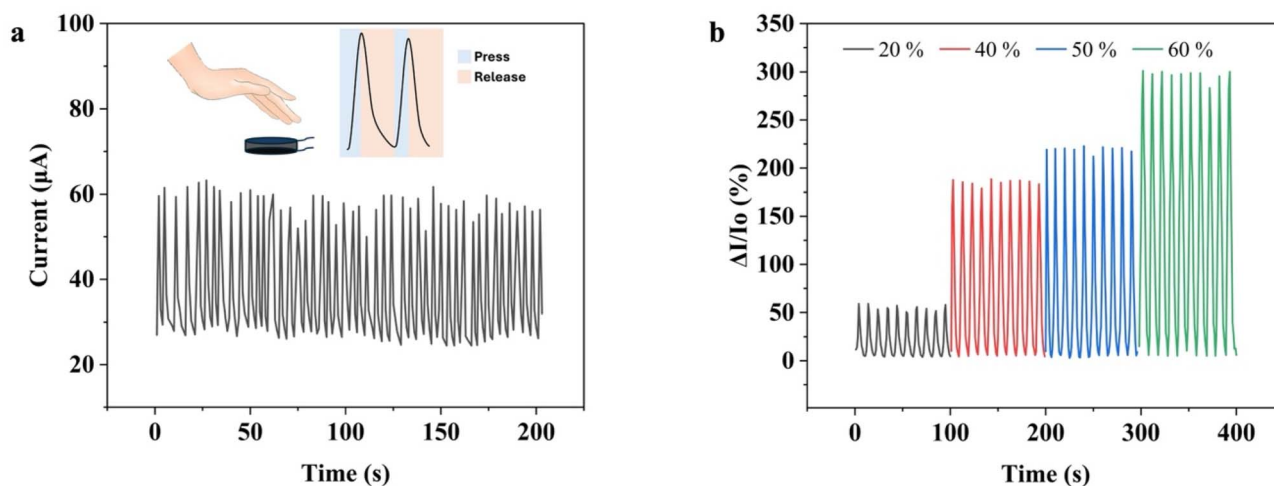
Fig. 6 (a) Testing of the MEG as a tactile sensor. (b) Current response of MEG to varying percentages of compressions.

centrosymmetric crystalline material) and triboelectric sensing (which requires contact electrification between dissimilar surfaces).

4. Conclusion

We have demonstrated a fundamentally new approach to fabricating high-performance MEGs based on a swelling gradient enabled by incorporated graphene-defined spheres. The electric output performance arises from the gradient size distribution of graphene-stabilized oil droplet sizes that arises from density differences in the oil-in-water emulsions used to template the MEGs. Our PAA hydrogels can generate a remarkably high-voltage output of 0.78 V. The MEGs were demonstrated to be effective across a wide range of temperatures, and MEG banks could be easily assembled with series and parallel configurations, generating substantial electrical energy capable of powering various electronic devices without the need for external rectifying circuits. Moreover, these MEGs can be utilized as self-powered tactile sensors for advancing human–machine interface technology.

5. Experimental

5.1 Materials

Natural graphite with a flake size of 3–5 μm (micro-850) was obtained from Ashbury Graphite Mills. Acrylic acid (TCI, 99%) and N,N'-methylenebis(acrylamide) (Sigma Aldrich, 99%), tannic acid (Alfa Aesar), ammonium persulphate (Fisher, 98%), lithium chloride (Sigma Aldrich, 99%), and n-heptane (Fisher, 99%) were all used as received. Metal electrodes, silver (thickness = 0.1 mm) and platinum (thickness = 0.05 mm), were purchased from Fisher Scientific.

5.2 Sample preparation

A glass jar (240 mL) was loaded with 15 mL of a 10% (by weight) acrylic acid aqueous solution, 0.1 g of N,N'-methylenebis(acrylamide) crosslinker, 15 mg tannic acid (1 mg tannic acid per ml water), 0.25 g lithium chloride, and 0.1 g ammonium persulfate initiator. The components were mixed well. Next, 15 mL of heptane was added, followed by 0.72 g of graphite. The jar was then sealed and shaken for two minutes using a bubble tea shaker (Happybuy Milk Tea shaker, 320 rpm). Finally, the jar was placed in a convection oven (Blue M, Stabil-Therm) at 65 °C for two hours to polymerize. Then, the sample was removed from the jar, and the bottom bulk poly (acrylic acid) layer was removed.

5.3 Characterization and measurement

System voltage responses were measured using a digital multimeter (Amprobe 38XR-A), and the data were recorded with Amprobe software. The current was recorded in real-time using a Keithley 2400 sourcemeter, which was controlled via a GPIB interface using PyVISA in Python. Commercial desiccants and a commercial humidifying chamber (AC infinity) were used to control humidity. Relative humidity was measured with a commercial hygrometer (Thermopro). An environmental chamber (Tenny) was used to control the temperature.

The morphology and composition of the as-prepared samples were investigated by a digital microscope (Olympus DSX1000). X-ray diffraction (XRD) patterns were recorded on a Bruker D2 PHASER diffractometer with a Cu Kα irradiation source ($\lambda = 1.54$ Å). Thermogravimetric analysis (TGA) was performed using a TA Instruments Q500 system under a nitrogen atmosphere. Differential scanning calorimetry (DSC) was conducted using a TA Instruments DSC Q20.

Conflicts of interest

The authors declare no conflicts of interest.

Data availability

All data supporting the findings of this study are provided in the main article and the supporting information (SI). Additional raw data, including voltage–time datasets, environmental stability measurements, microscopy images, and thermal analysis files, are available from the corresponding author upon request.

Supplementary information is available. See DOI: https://doi.org/10.1039/d5ta09936f.

Acknowledgements

References

1 M. Filonchyk, M. P. Peterson, L. Zhang, V. Hurynovich and Y. He, *Sci. Total Environ.*, 2024, **935**, 173359.

2 F. Perera, *Int. J. Environ. Res. Public Health*, 2017, **15**, 16.

3 X. Li, J. Tao, X. Wang, J. Zhu, C. Pan and Z. L. Wang, *Adv. Energy Mater.*, 2018, **8**, 1800705.

4 X. Gao, J. Wu, Y. Yu, Z. Chu, H. Shi and S. Dong, *Adv. Funct. Mater.*, 2018, **28**, 1706895.

5 Z. U. Khan, J. Edberg, M. M. Hamedi, R. Gabrielsson, H. Granberg, L. Wågberg, I. Engquist, M. Berggren and X. Crispin, *Adv. Mater.*, 2016, **28**, 4556.

6 T. Xu, X. Ding, C. Shao, L. Song, T. Lin, X. Gao, J. Xue, Z. Zhang and L. Qu, *Small*, 2018, **14**, 1704473.

7 J.-C. Feng, S.-X. Li, Z.-P. Zhang, Y. An, Q.-S. Gao, Z. Sun and H. Xia, *Nano Energy*, 2024, **119**, 109103.

8 A. Guchait, S. Pramanik, D. K. Goswami, S. Chattopadhyay and T. Mondal, *ACS Appl. Mater. Interfaces*, 2024, **16**, 46844.

9 J.-C. Feng, N. Wei, Z. Sun, S.-X. Li, X. Li and H. Xia, *Nano Energy*, 2024, **123**, 109409.

10 D. Shen, M. Xiao, G. Zou, L. Liu, W. W. Duley and Y. N. Zhou, *Adv. Mater.*, 2018, **30**, 1705925.

11 Y. Gao, A. Elhadad and S. Choi, *Small*, 2024, **20**, 2408182.

12 T. R. D. Ducati, L. H. Simões and F. Galembeck, *Langmuir*, 2010, **26**, 13763.

13 E. Fawole and W. D. Ristenpart, *Langmuir*, 2023, **39**, 17745.

14 Y. Huang, H. Cheng, C. Yang, H. Yao, C. Li and L. Qu, *Energy Environ. Sci.*, 2019, **12**, 1848.

15 S. Yang, L. Zhang, J. Mao, J. Guo, Y. Chai, J. Hao, W. Chen and X. Tao, *Nat. Commun.*, 2024, **15**, 3329.

16 F. Zhao, H. Cheng, Z. Zhang, L. Jiang and L. Qu, *Adv. Mater.*, 2015, **27**, 4351.

17 J. Xue, F. Zhao, C. Hu, Y. Zhao, H. Luo, L. Dai and L. Qu, *Adv. Funct. Mater.*, 2016, **26**, 8784.

18 J. Tan, S. Fang, Z. Zhang, J. Yin, L. Li, X. Wang and W. Guo, *Nat. Commun.*, 2022, **13**, 3642.

19 Z. Sun, X. Wen, L. Wang, D. Ji, X. Qin, J. Yu and S. Ramakrishna, *eScience*, 2022, **2**, 32.

20 Z. Huang, C. Li, W. Ying, N. Pan, X. Lei, J. Zhang, R. Wang and J. Wang, *Nano Energy*, 2024, **126**, 109673.

21 X. Gao, T. Xu, C. Shao, Y. Han, B. Lu, Z. Zhang and L. Qu, *J. Mater. Chem. A*, 2019, **7**, 20574.

22 Z. Huang, C. Li, W. Ying, N. Pan, X. Lei, J. Zhang, R. Wang and J. Wang, *Nano Energy*, 2024, **126**, 109673.

23 D. Maity and M. Fussenegger, *Advanced Science*, 2023, **10**, 2300750.

24 H. Wang, Y. Sun, T. He, Y. Huang, H. Cheng, C. Li, D. Xie, P. Yang, Y. Zhang and L. Qu, *Nat. Nanotechnol.*, 2021, **16**, 811.

25 K. Ni, Q. Ren, S. Liu, B. Sun, Y.-C. Lai, X. Zhang and R. Liu, *Energy Environ. Sci.*, 2024, **17**, 9406.

26 E. E. B. Brown, S. J. Woltornist and D. H. Adamson, *J. Colloid Interface Sci.*, 2020, **580**, 700.

27 S. J. Woltornist, J.-M. Y. Carrillo, T. O. Xu, A. V. Dobrynin and D. H. Adamson, *Macromolecules*, 2015, **48**, 687.

28 S. J. Woltornist, A. J. Oyer, J.-M. Y. Carrillo, A. V. Dobrynin and D. H. Adamson, *ACS Nano*, 2013, **7**, 7062.

29 R. Mohammadi Sejoubsari, T. O. Xu, S. P. Ward, N. M. Bandara, Z. Zhang and D. H. Adamson, *Soft Matter*, 2025, **21**, 1225.

30 S. J. Woltornist, J. M. Y. Carrillo, T. O. Xu, A. V. Dobrynin and D. A. Adamson, *Macromolecules*, 2015, **48**, 687.

31 S. J. Woltornist, A. J. Oyer, J.-M. Y. Carrillo, A. V. Dobrynin and D. H. Adamson, *ACS Nano*, 2013, **7**, 7062.

32 M. J. Joyce, S. T. McDermott, K. Umaiya and D. H. Adamson, *J. Colloid Interface Sci.*, 2024, **653**, 327.

33 Y. Huang, H. Cheng, C. Yang, P. Zhang, Q. Liao, H. Yao, G. Shi and L. Qu, *Nat. Commun.*, 2018, **9**, 4166.

34 X. Sui, H. Guo, C. Cai, Q. Li, C. Wen, X. Zhang, X. Wang, J. Yang and L. Zhang, *Chem. Eng. J.*, 2021, **419**, 129478.

35 A. L. P. Fernandes, R. R. Martins, C. G. Da Trindade Neto, M. R. Pereira and J. L. C. Fonseca, *J. Appl. Polym. Sci.*, 2003, **89**, 191.

36 J. J. Maurer, D. J. Eustace and C. T. Ratcliffe, *Macromolecules*, 1987, **20**, 196.

37 I. C. McNeill and S. M. T. Sadeghi, *Polym. Degrad. Stab.*, 1990, **29**, 233.

38 J. L. Bento, E. Brown, S. J. Woltornist and D. H. Adamson, *Adv. Funct. Mater.*, 2017, **27**, 1604277.

39 X. Wen, Z. Sun, X. Xie, Q. Zhou, H. Liu, L. Wang, X. Qin and S. C. Tan, *Adv. Funct. Mater.*, 2024, **34**, 2311128.

40 Z. Sun, L. Feng, C. Xiong, X. He, L. Wang, X. Qin and J. Yu, *J. Mater. Chem. A*, 2021, **9**, 7085.

41 J. Fang, X. Zhang, P. Duan, Z. Jiang, X. Lu, C. Fu, Y. Zhang, Y. Yao, K. Shang, J. Qin, Y. Liu and T. Yang, *Mater. Horiz.*, 2024, **11**, 1261.

42 X. Gao, T. Xu, C. Shao, Y. Han, B. Lu, Z. Zhang and L. Qu, *J. Mater. Chem. A*, 2019, **7**, 20574.

43 F. Horkay, *Gels*, 2021, **7**, 102.

44 A. R. Ranjbartoreh, B. Wang, X. Shen and G. Wang, *J. Appl. Phys.*, 2011, **109**, 014306.

45 O. L. Blakslee, D. G. Proctor, E. J. Seldin, G. B. Spence and T. Weng, *J. Appl. Phys.*, 1970, **41**, 3373.

46 C. Lee, X. Wei, J. W. Kysar and J. Hone, *Science*, 2008, **321**, 385.

47 Z. Bi, F. Gao, M. Liu, R. Zhang, R. Liu, G. Cui and J. Xu, *Chem. Eng. J.*, 2022, **450**, 138250.

48 T. Han, Z. Ma and D. Wang, *ACS Macro Lett.*, 2021, **10**, 354.

49 N. Bayliss and B. V. K. J. Schmidt, *Prog. Polym. Sci.*, 2023, **147**, 101753.

50 X. Liu, H. Gao, J. E. Ward, X. Liu, B. Yin, T. Fu, J. Chen, D. R. Lovley and J. Yao, *Nature*, 2020, **578**, 550.

51 M. Xia, N. Pan, C. Zhang, C. Zhang, W. Fan, Y. Xia, Z. Wang and K. Sui, *ACS Nano*, 2022, **16**, 4714.

52 X. Wen, Z. Sun, X. Xie, Q. Zhou, H. Liu, L. Wang, X. Qin and S. C. Tan, *Adv. Funct. Mater.*, 2024, **34**, 2311128.